

MAGNETIC FIELD STRENGTH IN THE UPPER SOLAR CORONA USING WHITE-LIGHT SHOCK STRUCTURES SURROUNDING CORONAL MASS EJECTIONS

R.-S. KIM^{1,3}, N. GOPALSWAMY^{1,3}, Y.-J. MOON², K.-S. CHO^{1,3,4}, AND S. YASHIRO^{1,3}

¹NASA Goddard Space Flight Center, Greenbelt, MD 20771, USA; rok-soon.kim@nasa.gov

²School of Space Research, Kyung Hee University, Yongin-shi 446-701, Republic of Korea

Received 2011 August 4; accepted 2011 November 14; published 2012 January 31

ABSTRACT

To measure the magnetic field strength in the solar corona, we examined 10 fast (≥ 1000 km s⁻¹) limb coronal mass ejections (CMEs) that show clear shock structures in *Solar and Heliospheric Observatory*/Large Angle and Spectrometric Coronagraph images. By applying the piston–shock relationship to the observed CME’s standoff distance and electron density compression ratio, we estimated the Mach number, Alfvén speed, and magnetic field strength in the height range 3–15 solar radii (R_s). The main results from this study are as follows: (1) the standoff distance observed in the solar corona is consistent with those from a magnetohydrodynamic model and near-Earth observations; (2) the Mach number as a shock strength is in the range 1.49–3.43 from the standoff distance ratio, but when we use the density compression ratio, the Mach number is in the range 1.47–1.90, implying that the measured density compression ratio is likely to be underestimated owing to observational limits; (3) the Alfvén speed ranges from 259 to 982 km s⁻¹ and the magnetic field strength is in the range 6–105 mG when the standoff distance is used; (4) if we multiply the density compression ratio by a factor of two, the Alfvén speeds and the magnetic field strengths are consistent in both methods; and (5) the magnetic field strengths derived from the shock parameters are similar to those of empirical models and previous estimates.

Key words: magnetic fields – methods: statistical – shock waves – Sun: corona – Sun: coronal mass ejections

Online-only material: color figures

1. INTRODUCTION

The solar corona is the plasma atmosphere of the Sun, extending millions of kilometers into space. One of the major issues of the solar corona is to measure the magnetic field, which determines the coronal structure and dynamics from the upper chromosphere out into the heliosphere. Evidence for the magnetic field in the corona has been found in several kinds of observations, but only a few of them give magnetic field information since the coronal plasma is optically thin (Wiegmann 2008). These observations are possible only in a limited spatial extent, and the magnetic field has to be derived with some uncertainties in interpretation.

One of the main techniques to estimate the coronal magnetic field is the optical observations of vector magnetic fields in the photosphere and their extrapolation into the corona. Lin et al. (2000) presented the magnetic field strength in the inner corona based on Stokes V circular polarization profiles. Solanki et al. (2003) reported a three-dimensional magnetic field topology in an interaction region near the base of the solar corona from the measurement of the Stokes vector. Their results for the magnetic field strength, B , are from tens to several hundreds of gauss in a very limited region ($r < 0.5 R_s$). The extrapolations of the photospheric magnetic field into the solar corona depend on assumptions such as low β plasma, which may not be valid in the outer corona (Gary 2001). Radio data may also be used as a diagnostic of the coronal magnetic structure. Lee et al. (1999) used radio observations of an active region to examine the coronal magnetic field obtained via a nonlinear force-free field extrapolation of a photospheric vector magnetogram. Ramesh

et al. (2010) showed that the estimated values of B at two different distances at 1.5 and 1.7 R_s from the observations of circularly polarized thermal radio emission from solar coronal streamers are 6 ± 2 G and 5 ± 1 G, respectively. It should be noted that the above techniques can be applied to measure the magnetic fields only in the inner corona ($r < 2 R_s$).

Several studies have been performed to measure magnetic fields in the corona from the band splittings in type II radio bursts (Smerd et al. 1974). Vrsnak et al. (2004) measured the interplanetary (IP) magnetic field strength using the band splitting of coronal and IP type II bursts, but they considered only four bins in the distance range of 25–225 R_s as a result of difficulties in the observation, such as a low signal-to-noise ratio and a small amount of data. Cho et al. (2007) used band splitting of coronal type II radio bursts and obtained a coronal magnetic field strength of 1.3–0.4 G in the height range of 1.5–2 R_s . Faraday rotation techniques have been occasionally used in estimating the magnetic field strengths at several solar radii (Patzold et al. 1987; Spangler 2005; Ingleby et al. 2007).

It is known that the observations in the solar corona approximately follow the empirical formulas $B(r) = 0.5(r/R_s - 1)^{-1.5}$ G for active regions (Dulk & McLean 1978) and $B(r) = 2.2(r/R_s)^{-2}$ G for quiet regions (Mann et al. 1999). Since these formulas were derived from observations of the lower corona below $\sim 10 R_s$, we may wonder whether these radial dependencies of B are still effective in the upper coronal region up to several tens of solar radii. The observations by the Large Angle and Spectrometric Coronagraph (LASCO) on board the *Solar and Heliospheric Observatory* (SOHO) satellite (Brueckner et al. 1995) enable us to study the upper corona in the range $1.5 R_s < r < 30 R_s$.

These observations have shown that the speeds of coronal mass ejections (CMEs) vary from a few hundred to more than 2500 km s⁻¹ (Yashiro et al. 2004; Gopalswamy 2010). CMEs

³ Department of Physics, The Catholic University of America, Washington, DC 20064, USA.

⁴ Korea Astronomy and Space Science Institute, Daejeon, Republic of Korea.

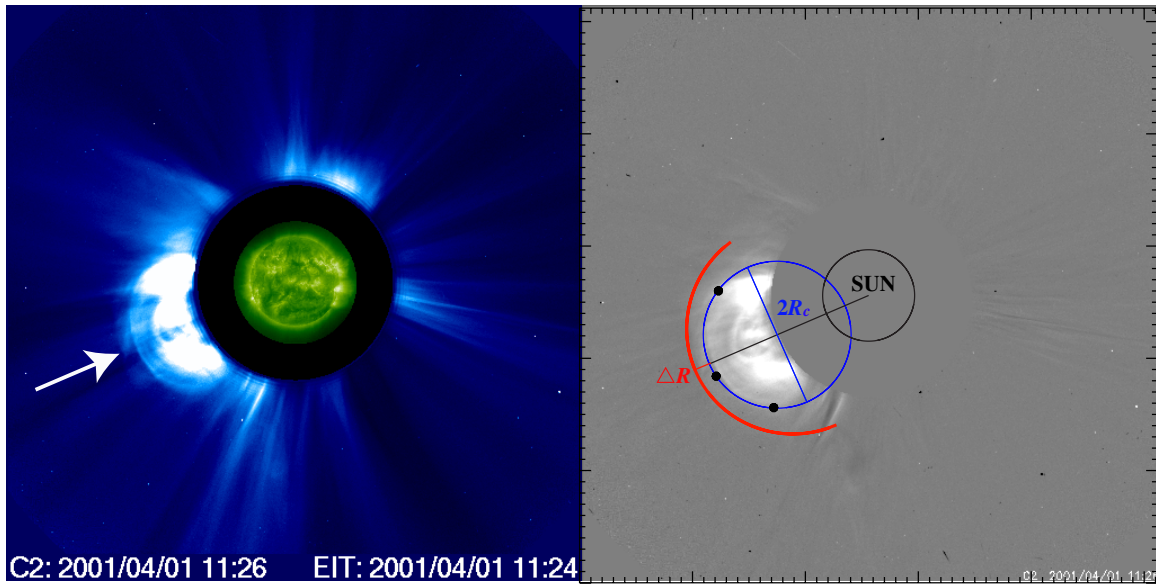


Figure 1. Left panel shows a *SOHO*/LASCO image of the 2001 April 1 CME at 11:26 UT showing the diffuse structure ahead of the CME flux rope (the sharp feature). The arrow indicates the shock nose. The right panel shows the running difference image of the event. The radial black line marks the central P.A. of the shock nose, and the blue circle indicates the CME as an obstacle. The red lines indicate the shock front and standoff distance, ΔR .

(A color version of this figure is available in the online journal.)

with speeds in excess of the ambient Alfvén speed, which is characterized by the magnetic field and plasma density, may drive fast-mode magnetohydrodynamic (MHD) shocks. As a shock signature associated with CMEs, streamer deflections have been suggested and observed (Gosling et al. 1974; Michels et al. 1984; Sheeley et al. 2000). Recently, several studies have shown that the CME-driven shocks could be directly observed in white-light coronagraph images, under suitable conditions from the analysis of white-light (Vourlidas et al. 2003; Gopalswamy et al. 2009a; Ontiveros & Vourlidas 2009; Bemporad & Mancuso 2010; Gopalswamy 2010) and EUV (Gopalswamy et al. 2012; Ma et al. 2011; Kozarev et al. 2011) images, as well as from MHD simulations (Stepanova & Kosovichev 2000; Manchester et al. 2004). If these structures are truly shocks, there should be noticeable rapid rises in pressure, temperature, and density of the flow that are applicable to the piston–shock relationship (Eselevich & Eselevich 2010).

In piston-driven shocks such as Earth’s bow shock, there are several parameters that can govern the shock shapes: the size and shape of the obstacle, the electron density compression ratio, the upstream Mach number, and the standoff distance (the distance between the obstacle and its shock nose). Russell & Mulligan (2002) applied the relation between shock standoff distance and a CME near Earth to explain the curvature of the driving IP CME. Gopalswamy & Yashiro (2011) measured the standoff distance of a CME-driven shock in the corona using *SOHO*/LASCO and the *Solar Terrestrial Relations Observatory* images and derived a coronal magnetic field in the range of 6–23 R_s .

In this paper, we consider a large number of shock-driving CMEs identified in the *SOHO*/LASCO images and use the standoff distance technique (Gopalswamy & Yashiro 2011) to measure the coronal magnetic field. Following the case study of Gopalswamy & Yashiro (2011), we estimate the magnetic field radial distributions in the upper corona using the standoff distance technique. We also use the density compression ratio across the shock to determine the magnetic field and compare the results with those from the standoff distance technique. In

addition, we compare the magnetic field distributions with those in previous studies. We also examine the physical properties of the upstream medium from different techniques for consistency. The paper is organized as follows. The data and methodology are described in Section 2. In Section 3, we present estimations of the coronal Alfvén speeds and magnetic field strengths using the standoff distance and the density compression ratio methods. A summary and conclusions are given in Section 4.

2. DATA AND METHODOLOGY

2.1. Data Selection

For the analysis of CME-driven shocks, we selected good candidates that show clear signatures of discontinuity ahead of the CMEs as they propagate from the Sun. The left panel of Figure 1 shows an example of the shock structure observed by *SOHO*/LASCO. The shock structure appears as a diffuse feature surrounding the CME as indicated by the arrow. Assuming that the leading edge of the diffuse structure is the piston-driven shock, we measure shock parameters such as the standoff distance and electron density compression ratio as indicators of the shock strength.

To select a sample of CME-driven shock structures, we used the following procedure: (1) we selected fast CMEs (≥ 1000 km s $^{-1}$) from 1996 to 2007 using the *SOHO*/LASCO online CME catalog⁵ (Yashiro et al. 2004; Gopalswamy et al. 2009b), since these CMEs are fast enough to drive shocks (see Gopalswamy et al. 2008c); (2) we checked only CMEs associated with M- and X-class solar flares whose source locations are close to the limb ($>60^\circ$) to minimize projection effects; (3) we used events that show clear shock structures in at least three frames within C2 and/or C3 fields of view. Although we identified 104 CMEs with shock structures, many were too faint to measure the standoff distance or they have only one or two frames that show shock signatures. We also excluded CMEs which had preceding CMEs within 12 hr, since the pre-events

⁵ http://cdaw.gsfc.nasa.gov/CME_list/index.html

Table 1
Information about Very Fast ($\geq 1000 \text{ km s}^{-1}$) Limb CMEs that Show Clear Shock Structures from 1997 to 2003

No.	CME Date/Time	Type II ^a Time	Shock Position		Shock Parameter			Mach No.		V_A (km s ⁻¹)		B (mG)	
			P.A. (°)	Height (R_s)	$\Delta R/R_c$	ρ_d/ρ_u	V_{SH} (km s ⁻¹)	$M_{\Delta R}$	M_ρ	$V_{\Delta R}$	$V_{A\rho}$	$B_{\Delta R}$	B_ρ
1	1997 Nov 14 10:14:03	No	70	3.33	0.78	1.35	862	1.49	1.63	580	527	101	92
	1997 Nov 14 10:52:30		67	6.19	0.35	1.12	988	2.09	1.53	471	647	27	37
2	1999 Jul 25 13:31:21	13:21 M	301	3.08	0.27	1.30	1259	2.51	1.61	501	780	105	163
	1999 Jul 25 13:54:05		301	5.55	0.38	1.22	1370	2.00	1.58	684	869	46	58
	1999 Jul 25 14:18:05		301	8.50	0.53	1.08	1546	1.71	1.51	902	1025	34	38
	1999 Jul 25 14:42:05		301	11.7	0.54	1.05	1400	1.70	1.49	825	937	21	24
3	2000 Apr 4 16:43:01	15:31 M	325	11.46	0.55	1.01	1279	1.68	1.48	761	867	20	23
	2000 Apr 4 17:18:06		326	15.33	0.34	1.00	1049	2.12	1.47	494	711	10	14
4	2000 May 4 11:42:05	11:06 M	226	7.92	0.61	1.14	705	1.62	1.53	435	459	18	19
	2000 May 4 12:42:05		226	12.64	0.20	1.07	1142	3.20	1.51	356	758	8	18
5	2000 May 5 16:18:05	16:35 D	213	6.35	0.37	1.17	1308	2.03	1.55	643	843	35	46
	2000 May 5 16:42:06		214	9.06	0.33	1.12	1299	2.16	1.53	601	851	21	29
6	2000 Jun 15 20:26:06	19:43 M	306	6.06	0.31	1.08	761	2.25	1.51	338	504	20	29
	2000 Jun 15 20:42:05		307	7.11	0.33	1.07	1030	2.17	1.51	473	683	22	32
	2000 Jun 15 21:18:05		307	10.31	0.25	1.06	947	2.59	1.50	365	632	11	19
	2000 Jun 15 21:42:05		308	12.27	0.19	1.04	889	3.43	1.49	258	596	6	15
7	2001 Apr 1 11:26:06	No	116	4.21	0.27	1.33	1197	2.45	1.62	488	737	52	79
	2001 Apr 1 11:50:07		117	6.69	0.24	1.12	1318	2.69	1.53	490	861	25	44
8	2001 Dec 28 20:30:05	19:59 M	151	5.98	0.33	1.19	2132	2.17	1.56	981	1366	58	81
	2001 Dec 28 21:18:32		152	14.89	0.25	1.10	2067	2.62	1.52	788	1360	16	27
9	2002 Jan 14 06:05:05	06:08 M	220	4.82	0.25	1.91	1461	2.66	1.90	549	768	46	64
	2002 Jan 14 06:30:05		220	7.78	0.20	1.33	1762	3.19	1.63	551	1083	23	45
	2002 Jan 14 06:45:05		220	10.06	0.22	1.29	1621	2.97	1.61	545	1008	17	31
	2002 Jan 14 07:00:06		218	12.16	0.21	1.21	1818	3.04	1.57	598	1159	15	29
10	2003 Oct 24 03:06:06	No	124	3.56	0.20	1.25	1228	3.28	1.59	373	773	56	117
	2003 Oct 24 03:30:05		124	6.10	0.22	1.18	1048	2.92	1.56	358	672	21	39

Notes. ^a M: Metric type II radio burst; D: DH type II radio burst.

could significantly disturb the ambient conditions including the upstream density and the Alfvén speed (Eselevich & Eselevich 2011). Finally, we selected only 26 frames corresponding to 10 events that show relatively clear shock features. These events mainly occurred during the solar maximum phase of solar cycle 23. Table 1 summarizes the basic information about these events. We also list the occurrence of metric and/or decameter-hectometric (DH) type II radio bursts in the third column since a shock in the leading edge of the CME could be the source of a type II radio burst (Gopalswamy et al. 2005; Cho et al. 2011).

2.2. Standoff Distance Ratio

The standoff distance, ΔR , in the CME-driven shock structure is defined as the distance from the front of a CME to its shock nose in the radial direction, as shown in the right panel of Figure 1. The standoff distance of a strong shock is shorter than that of a weak shock when we consider the same CME size. Since the standoff distance is proportional to the size of the CME (Russell & Mulligan 2002; Manchester et al. 2004), we measured the curvature radius of the CME, R_c , and determined the ratio of ΔR to R_c as an indicator of the shock strength. ΔR and R_c can be determined directly from the coronagraph images. The measurement of the standoff distance ratio, $\Delta R/R_c$, is made as follows: (1) to determine R_c , we fitted a circle to the CME front in the *SOHO*/LASCO running difference image (see the blue circle in the right panel of Figure 1); (2) we then measured the distance from the CME front and the leading edge of the diffuse structure in the radial direction as ΔR (red straight line); (3) we

considered the position of the shock nose as the shock height. The central position angle (P.A.) of the CMEs, the shock height, and $\Delta R/R_c$ are listed in the fourth, fifth, and sixth columns of Table 1, respectively, for the 10 events.

Figure 2 shows the variation of $\Delta R/R_c$ with heliocentric distance for the 10 events, roughly scattered in the range 0.19–0.78 (mean = 0.34) at the height range from 3.1 to 15.3 R_s . We included the standoff distance ratios for a single event from Gopalswamy & Yashiro (2011), indicated by red circles. For comparison, we have also plotted the standoff distances of seven magnetic clouds (MCs) observed at near-Earth IP space, which are selected from the MC list of Gopalswamy et al. (2008a) satisfying the condition $10^\circ \text{ E} < \text{Longitude} < 10^\circ \text{ W}$ to confirm that they pass the Earth by their noses. We calculated the standoff distances using the time difference of IP shock and sheath and the MC's speed information from the list, and we assumed that the radius of the MC's curvature is 0.4 AU as suggested by Russell & Mulligan (2002). As a result, the mean of the standoff distance ratio for seven MCs is 0.33, which is similar to that of near-Sun shocks (see Maloney & Gallagher 2011). The standoff distances are the same (0.22) for two events, so the data points overlapped in Figure 2.

We also compared our result with the standoff distance ratio of Manchester et al. (2004), who presented a three-dimensional numerical ideal MHD model describing the time-dependent expulsion of a CME. According to their simulation, the standoff distance of the shock is 4.3 R_s when the CME's front is at 40 R_s . Then the shock front reaches 1 AU ($\sim 215 R_s$) 16 R_s ahead of the CME. At the two distances of 44.3 R_s and 215 R_s , the ratios

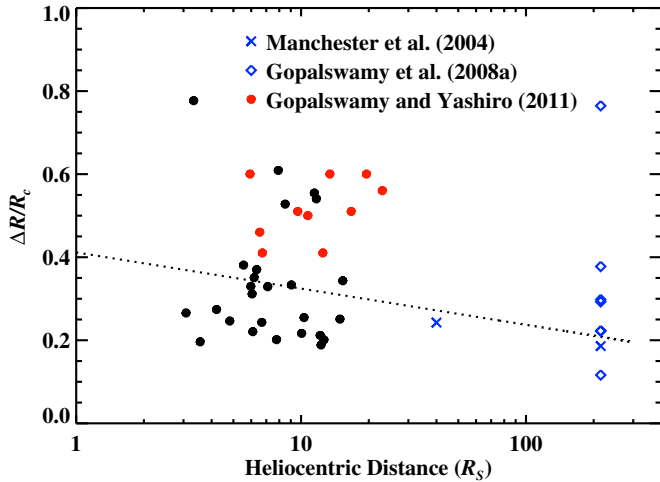


Figure 2. Heliocentric distribution of the standoff distance ratio, $\Delta R/R_c$, for 26 shock positions of 10 CMEs indicated by black circles. The x -axis is the height of the shock position, and the y -axis is $\Delta R/R_c$. The dotted line presents the polynomial fit, and the red circles indicate the standoff distance ratios for a single event from Gopalswamy & Yashiro (2011). Diamonds and crosses are the standoff distance ratios from MC observations and the numerical model, respectively.

(A color version of this figure is available in the online journal.)

of the standoff distance are 0.27 and 0.19, respectively, when we take $R_c = 0.4r$, where r is the heliocentric distance of the CME (Russell & Mulligan 2002). We also added their results to Figure 2. As shown in the figure, our $\Delta R/R_c$ values are comparable to those from the numerical CME model and near-Earth observations.

2.3. Electron Density Compression Ratio

One of the quantities needed in the estimation of the coronal magnetic field is the upstream electron density, which can be estimated from the inversion of polarized brightness (pB) measurements (Gopalswamy & Yashiro 2011). Van de Hulst (1950) derived a parametric representation for the electron density, ρ , as a function of the radial distance from the Sun. This method has been widely applied to obtain radial profiles of the coronal electron density from calibrated white-light images. Hayes et al. (2001) extended the Van de Hulst (VDH) method to take advantage of the extensive LASCO archive of total brightness (tB) images. pB images are obtained only twice a day, while tB images are obtained with a much higher cadence.

To measure the downstream/upstream electron density compression ratio, we adopted the method of Hayes et al. (2001) to LASCO C2 and C3 tB images instead of pB images since it is very hard to obtain the density compression ratio by using the pB images, which have a very poor time cadence (two to three frames per day). The detailed procedure to obtain the density compression ratio is as follows: (1) for each frame, we selected LASCO/C2 and C3 images, which are in the time window starting 4 hr before the associated eruption and ending 4 hr after the last CME observation; (2) we plotted the radial profile of the electron density at the P.A. corresponding to the nose of the shock; (3) we measured the electron density at the shock height in the radial profile.

Figure 3 shows the temporal variation of the density for a given shock height for the 2001 April 1 event. This figure shows the density jump after the CME's first appearance, indicated by the arrow. We calculated the downstream/upstream electron

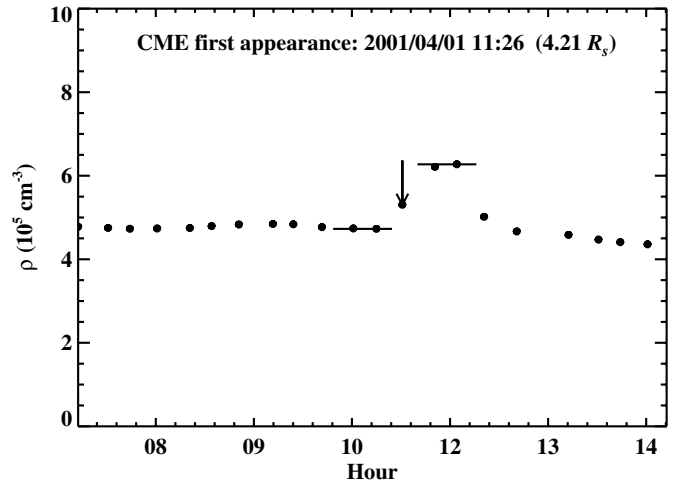


Figure 3. Example of the temporal variation of electron density at the shock position. The arrow indicates the CME's first appearance time, and the two solid lines show the upstream (left) and downstream (right) electron densities.

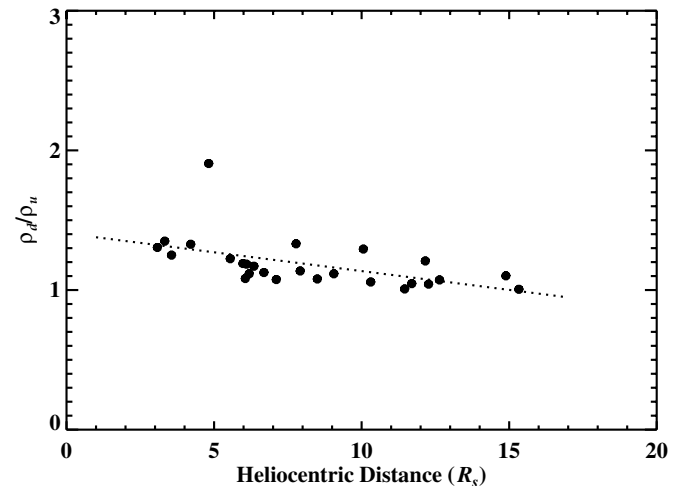


Figure 4. Downstream/upstream electron density compression ratio, ρ_d/ρ_u , as a function of the heliocentric distance. The dotted line is the polynomial fit to the compression ratio.

density compression ratio by dividing the maximum electron density, ρ_d , by the average of upstream electron densities, ρ_u , as marked by the solid lines. We assumed a nominal depth of $1 R_s$ for all the events because it is a convenient scale and is likely a good upper limit (Ontiveros & Vourlidis 2009). The density compression ratios for the 10 events are in the range 1.00–1.91 (mean = 1.18) as shown in Figure 4 and Table 1. In the inner region below $5 R_s$, the compression ratio is relatively higher than that in the outer region, but it is still low and the ratio is close to 1 as the heliocentric distance increases, as indicated by the polynomial fitting result (dotted line). This result shows a different tendency from Figure 8 of Eselevich & Eselevich (2011), which shows that the density compression ratio increases with distance. We speculate that the difference is from the shock size l along the line of sight. They assumed l as $6.5 R_s$, while we used $1 R_s$. Note that their average shock height ($18.6 R_s$) is substantially higher than ours ($8.2 R_s$).

2.4. Shock Speed

We determined the shock speeds, V_{SH} , at 26 shock positions by subtracting the ambient solar wind speed from the upstream shock speed, which is measured from two successive frames.

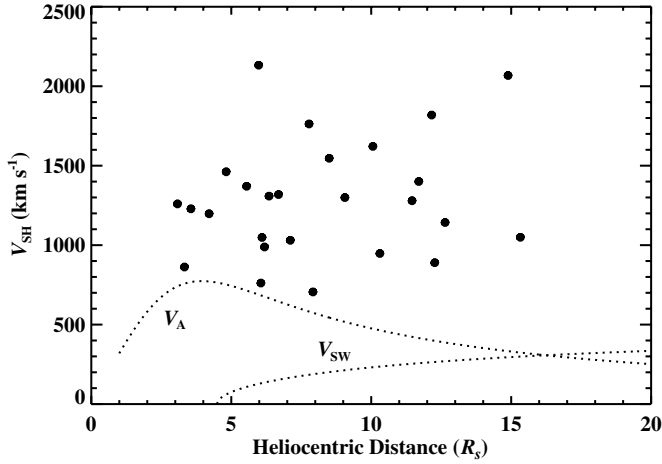


Figure 5. Distribution of the shock speeds, V_{SH} . The dotted lines show the variations of the Alfvén speed and the solar wind speed as a function of the heliocentric distance.

The distribution of the shock speed is shown in Figure 5. The shock speed ranges from 705 to 2132 km s⁻¹ (mean = 1288 km s⁻¹). The solar wind speed profile was taken from the empirical relation obtained by Sheeley et al. (1997). To compare with the Alfvén speed, we added the Alfvén speed profile obtained using the models of magnetic field and plasma density (Dulk & McLean 1978; LeBlanc et al. 1998; Mann et al. 1999; Gopalswamy et al. 2001; Eselevich & Eselevich 2008). As shown in the figure, all events have speeds faster than the Alfvén speeds and hence can form shocks. We have also listed the shock speeds, V_{SH} , in the eighth column of Table 1.

2.5. Shock Mach Number

It is well known that the density compression ratio is related to the compressibility of the medium and the upstream Mach number (Landau & Lifshitz 1959). According to a modified method suggested by Farris & Russell (1994) for low Mach numbers (weak shock), the density compression ratio is expressed by

$$\frac{\rho_d}{\rho_u} = \frac{(\gamma + 1)(M^2 - 1)}{(\gamma - 1)M^2 + 2}, \quad (1)$$

where γ is the ratio of specific heats and M is the upstream Mach number. Seiff (1962) showed empirically that the standoff distance of a bow shock, which is normalized by the radius of the obstacle, is linearly proportional to the inverse density ratio. Then Farris & Russell (1994) modified this relationship to consider the radius of curvature (R_c) of the obstacle, and the standoff distance ratio can be given by

$$\frac{\Delta R}{R_c} = 0.8 \frac{\rho_u}{\rho_d}. \quad (2)$$

This yields a relationship between the standoff distance ratio and the Mach number:

$$\frac{\Delta R}{R_c} = 0.8 \frac{(\gamma - 1)M^2 + 2}{(\gamma + 1)(M^2 - 1)}, \quad (3)$$

which indicates that for a weak shock, as M increases, the standoff distance ratio decreases.

If we measure the standoff distance ratio and the density compression ratio, we can calculate the upstream Mach number

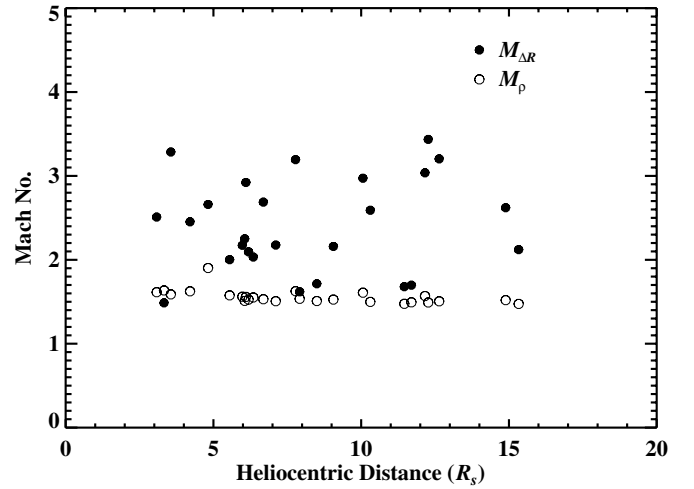


Figure 6. Heliocentric distribution of Mach numbers calculated using Equations (4) and (5). The filled circles indicate the Mach numbers from the standoff distance ratio, $M_{\Delta R}$, and the empty circles indicate those from the density compression ratio, M_{ρ} .

by rewriting Equations (3) and (1) as

$$M_{\Delta R}^2 = \frac{\Delta R/R_c(\gamma + 1) + 1.6}{\Delta R/R_c(\gamma + 1) - 0.8(\gamma - 1)} \quad (4)$$

and

$$M_{\rho}^2 = \frac{2\rho_d/\rho_u + \gamma + 1}{\gamma + 1 - \rho_d/\rho_u(\gamma - 1)}, \quad (5)$$

where γ is assumed to be 4/3 (Liu et al. 2006; Gopalswamy & Yashiro 2011).

We calculated the Mach number from both methods: (1) from the standoff distance ratio, $M_{\Delta R}$, and (2) from the density compression ratio, M_{ρ} . Figure 6 shows the Mach numbers determined by Equations (4) and (5) for the 26 shock positions in the 10 CMEs. $M_{\Delta R}$ is randomly scattered in the range 1.49–3.43 with a mean value of 2.41, but M_{ρ} occupies a narrow range of 1.47–1.90 with a mean value of 1.56. We list $M_{\Delta R}$ and M_{ρ} in the ninth and tenth columns of Table 1, respectively. If we set γ as 5/3, then the denominators of Equations (4) and (5) are close to or below 0 for very strong shocks ($\Delta R/R_s \leq 0.2$ or $\rho_d/\rho_u \geq 4$), which makes the Mach number unrealistically high.

3. RESULTS

3.1. Alfvén Speed

Since we estimated the upstream Mach numbers from the standoff distance ratio and the density compression ratio, the Alfvén speed is easily determined using the simple relation

$$V_A = \frac{V_{SH}}{M}, \quad (6)$$

where V_A is the upstream Alfvén speed.

Figure 7 shows the distribution of Alfvén speeds determined by Equation (6) using the standoff distance (filled circles) and the density compression (empty circles) methods. The Alfvén speeds from the standoff distance ratio, $V_{A\Delta R}$, are roughly scattered in the range 259–982 km s⁻¹ (mean = 555 km s⁻¹), and from the density compression ratio the Alfvén speeds, $V_{A\rho}$, are in the range 459–1367 km s⁻¹ (mean = 826 km s⁻¹). These values are consistent with the factor of three variation in the

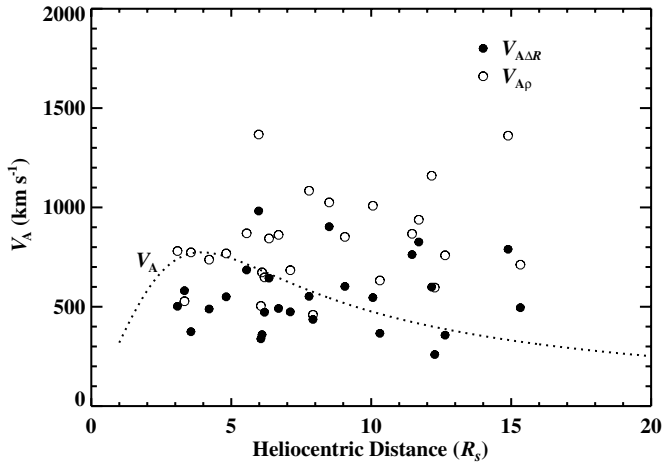


Figure 7. Heliocentric distribution of Alfvén speeds using the standoff distance ratio, $V_{A\Delta R}$, and the density compression ratio, $V_{A\rho}$. The dotted line indicates the Alfvén speed from the model (see Gopalswamy et al. 2001; Eselevich & Eselevich 2008).

Alfvén speed derived from radio-quiet and radio-loud CMEs (Gopalswamy et al. 2008b, 2008c). As seen in the figure, $V_{A\rho}$ values are much higher than the $V_{A\Delta R}$ values. We list the Alfvén speeds $V_{A\Delta R}$ and $V_{A\rho}$ in the eleventh and twelfth columns of Table 1, respectively.

3.2. Magnetic Field Strength

The Alfvén speed is defined as

$$V_A = 2 \times 10^6 \rho^{-1/2} B \text{ (km s}^{-1}\text{)}, \quad (7)$$

where the magnetic field strength, B , can be determined using

$$B = \frac{1}{2} \times 10^{-6} V_A \rho^{1/2} \text{ (G)}. \quad (8)$$

To estimate the magnetic field strength in the upper solar corona, we used the Alfvén speeds obtained from the standoff distance ratios and the density compression ratios. The other parameter needed in Equation (8) is the upstream plasma density, which can be obtained in a number of ways. Gopalswamy & Yashiro (2011) used the density at the nose obtained from the pB images. Gopalswamy et al. (2012) used the plasma density given by the lower frequency branch in type II band splitting. Since we were not able to get appropriate pB images for all 10 events, we decided to use a density model. We used the density model of LeBlanc et al. (1998):

$$\rho(r) = 3.3 \times 10^5 r^{-2} + 4.1 \times 10^6 r^{-4} + 8.0 \times 10^7 r^{-6}. \quad (9)$$

Figure 8 shows the magnetic field strengths in the upstream region through which the 10 fast limb CMEs propagate. The magnetic field strengths in the upper solar corona (3–15 R_s) are distributed from 105 to 6 mG (mean = 32 mG) based on the standoff distance ratio. When the density compression ratios are used, B is between 163 and 14 mG (mean = 47 mG). The distribution of $B_{\Delta R}$ is consistent with the Dulk & McLean (1978) empirical model, while the distribution of B_ρ is substantially higher than $B_{\Delta R}$. For comparison we included the magnetic field strengths from previous studies (Patzold et al. 1987; Spangler 2005; Cho et al. 2007; Ingleby et al. 2007; Bemporad & Mancuso 2010). We also plotted the result from 2008 March 25 using the standoff distance technique (Gopalswamy & Yashiro

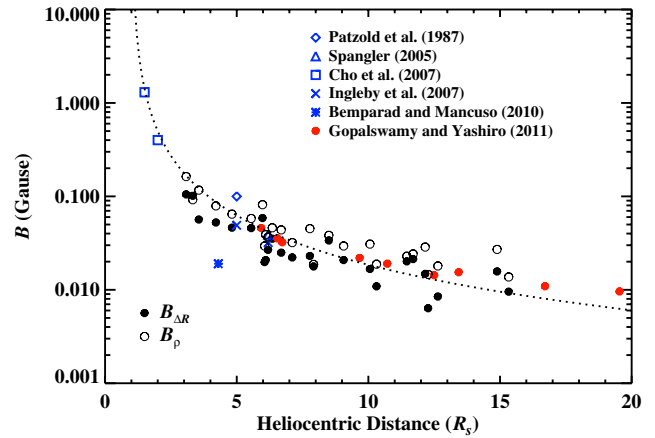


Figure 8. Magnetic field strength using the standoff distance ratio, $B_{\Delta R}$, and the density compression ratio, B_ρ , as a function of heliocentric distance. The dotted line indicates the empirical magnetic field model (Dulk & McLean 1978).

(A color version of this figure is available in the online journal.)

2011). We list the magnetic field strengths from the standoff distance ratio and the density compression ratio in the final two columns of Table 1. We note that this kind of shock analysis can be adapted to measure the magnetic field strength in the solar corona and to interpret the CME-driven shock structure.

3.3. Comparison of Shock Parameters

As shown in Figure 8, the magnetic field strengths derived from the density compression ratio are higher than those derived from the empirical model and the standoff distance ratio. We speculate that the density compression ratio might be underestimated as a result of contributions from the background density. That is, it is hard to distinguish the enhanced electron density from the background electron density accumulated along the line of sight, especially in the upper coronal region. Regarding this argument, Figure 4 shows that the observed density enhancement decreases as the heliocentric distance increases. Several authors have attempted to get a more accurate density compression ratio by assuming the shock size l along the line of sight (Ontiveros & Vourlidis 2009; Eselevich & Eselevich 2011). It is noted that the standoff distance measurements have no such weakness. In fact, the density compression ratio obtained from type II burst band splitting has been shown to agree with the standoff distance method. Therefore, we think that the uncertainty in the compression ratio obtained from white-light observations comes mainly from the assumption of the line-of-sight depth of the shock.

In order to account for the underestimation of the density compression ratio, we multiplied the compression ratio by a factor of two. The resulting Alfvén speeds are shown in Figure 9. The comparison shows that the Alfvén speeds are consistent with each other with a correlation coefficient of 0.74 when the twofold density compression ratio is used. Figure 10 shows the comparison between the magnetic field strength from the standoff distance ratio and those from the original and twofold density compression ratios. The magnetic field strengths from both methods are very consistent with each other with a correlation coefficient of 0.92 when the twofold density ratio is used.

4. SUMMARY AND CONCLUSION

To measure the magnetic field strength in the solar corona, we examined 10 fast ($\geq 1000 \text{ km s}^{-1}$) limb CMEs that show

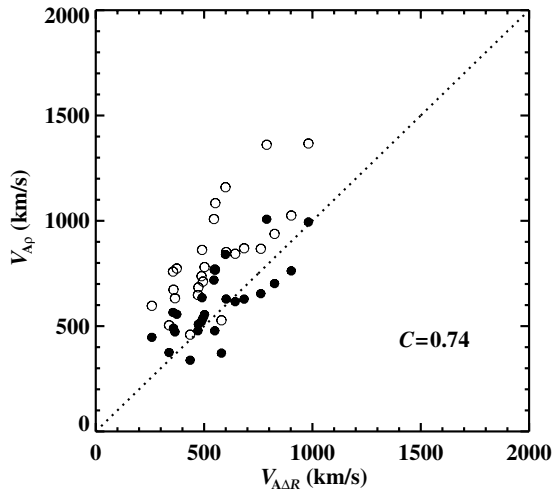


Figure 9. Relationship between the Alfvén speeds from the standoff distance ratio and the density compression ratios when we take the original and twofold density compression ratios. The filled circles indicate the values using the twofold density compression ratio and the empty circles indicate those from the original density compression ratio. The dotted line indicates when the Alfvén speeds are the same in both methods.

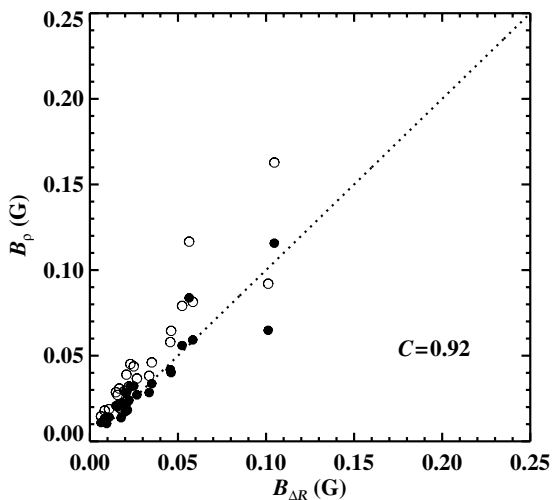


Figure 10. Relationship between the magnetic field strengths from the standoff distance ratio and the density compression ratio methods when we take the original and twofold density compression ratios. The explanations are the same as in Figure 9.

clear shock structures in *SOHO*/*LASCO* images. By applying the piston–shock relationship to the observed CME’s standoff distance, we obtained a coronal Alfvén speed ranging from 259 to 982 km s^{−1} and a magnetic field strength ranging from 6 to 105 mG in the heliocentric distance range of 3–15 R_s . The magnetic field strength is consistent with the empirical models (Dulk & McLean 1978) and other studies (Patzold et al. 1987; Spangler 2005; Cho et al. 2007; Ingleby et al. 2007; Bemporad & Mancuso 2010; Gopalswamy & Yashiro 2011). These results confirm that the standoff distance ratio provides us with a useful tool to derive magnetic fields over a wide range of the solar corona ($\sim 30 R_s$).

The Alfvén speeds and magnetic field strengths derived from the density compression ratio are about two times higher than the results above. We speculate that the density compression ratio obtained from white-light observations might be underestimated since the observed density is based on electrons integrated

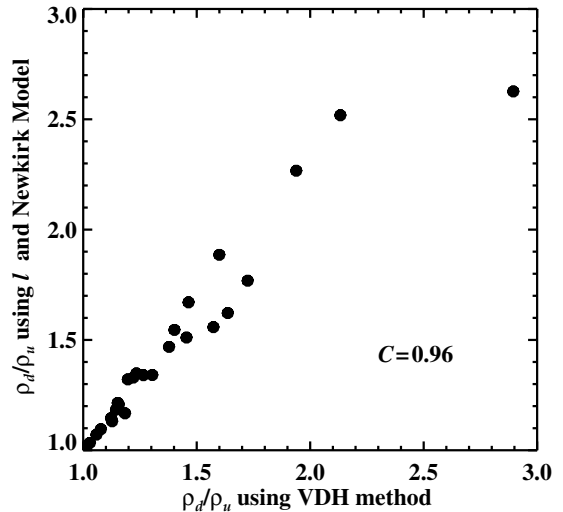


Figure 11. Correlation between previous ρ_d/ρ_u values based on the VDH method and new ρ_d/ρ_u values based on the l and Newkirk density model.

over the line of sight, while the measurements of the standoff distance ratio have no such weakness. To inspect the line-of-sight effect on the density compression ratio, we adopted the method proposed by Eselevich & Eselevich (2011), which uses the differential brightness (dP) from the *LASCO* tB image and the shock size l along the line of sight. Assuming that the CME and shock’s configuration are symmetric, we measured the length of the tangential line at the CME’s nose, which is considered equivalent to the length along the line of sight, l . As a result, we found that if we choose the Newkirk density model (Newkirk 1961) for the upstream density, the density compression ratio, which is calculated from dP and l , has a very good correlation with our previous result from the VDH method with a correlation coefficient of 0.96, as shown in Figure 11.

We also note that when we multiply the density compression ratio by a factor of two the Alfvén speeds and magnetic field strengths are consistent with those from the standoff distance technique. This supports the idea that the diffuse structures surrounding the CME front, as shown in Figure 1, can be interpreted as shock structures—shock sheaths, to be precise. There are two main observational results that support the existence of shocks in the low corona. Type II radio bursts in the metric (Cliver et al. 1999) and longer wavelengths (Gopalswamy et al. 2005) are good indicators near the Sun. The white-light observations of diffuse features surrounding the CME flux ropes confirm this, as inferred from streamer deflections (Gosling et al. 1974) and other white-light signatures (Vourlidis et al. 2003; Sheeley et al. 2000; Gopalswamy et al. 2008c, 2009a) and MHD simulations (Manchester 2009).

Finally, we would like to stress the fact that this study is a new attempt (together with Gopalswamy & Yashiro 2011) to measure the magnetic field strengths in the upper corona up to 30 R_s by applying the piston–shock relationship to CME coronagraph observations. This method can be applied to CMEs showing clear shock structures surrounding the CME front so that it can provide us with a useful method to derive the magnetic fields in the solar corona. It is a unique method to derive magnetic fields in the upper solar corona (10–20 R_s).

Y.-J.M. has been supported by the WCU program (No. R31-10016) and Basic Research Promotion Fund (20090071744 and 20100014501) through the National Research Foundation

of Korea funded by the Ministry of Education, Science and Technology. K.-S.C. is supported by the Development of Korean Space Weather Center, a project of KASI, and the KASI basic research fund.

REFERENCES

- Bemporad, A., & Mancuso, S. 2010, *ApJ*, **720**, 130
- Brueckner, G. E., Howard, R. A., Koomen, M. J., et al. 1995, *Sol. Phys.*, **162**, 357
- Cho, K.-S., Bong, S.-C., Moon, Y.-J., et al. 2011, *A&A*, **530**, A16
- Cho, K.-S., Lee, J., Gary, D. E., Moon, Y.-J., & Park, Y. D. 2007, *ApJ*, **665**, 799
- Cliver, E. W., Webb, D. F., & Howard, R. A. 1999, *Sol. Phys.*, **187**, 89
- Dulk, G. A., & McLean, D. J. 1978, *Sol. Phys.*, **57**, 279
- Eselevich, M., & Eselevich, V. 2008, *Geophys. Res. Lett.*, **35**, L22105
- Eselevich, M., & Eselevich, V. 2010, arXiv:1004.1859
- Eselevich, M., & Eselevich, V. 2011, *Astron. Rep.*, **55**, 359
- Farris, M. H., & Russell, C. T. 1994, *J. Geophys. Res.*, **99**, 17681
- Gary, G. A. 2001, *Sol. Phys.*, **203**, 71
- Gopalswamy, N. 2010, in Proc. 20th National Solar Physics Meeting, ed. I. Dorotovi (Slovakia: Papradno), 108
- Gopalswamy, N., Aguilar-Rodriguez, E., Yashiro, S., et al. 2005, *J. Geophys. Res.*, **110**, A12
- Gopalswamy, N., Akiyama, S., Yashiro, S., Michalek, G., & Lepping, R. P. 2008a, *J. Atmos. Sol.-Terr. Phys.*, **70**, 245
- Gopalswamy, N., Lara, A., Kaiser, M. L., & Bougeret, J.-L. 2001, *J. Geophys. Res.*, **106**, 25261
- Gopalswamy, N., Nitta, N., Akiyama, S., Makela, P., & Yashiro, S. 2012, *ApJ*, **744**, 72
- Gopalswamy, N., Thompson, W. T., Davila, J. M., et al. 2009a, *Sol. Phys.*, **259**, 227
- Gopalswamy, N., & Yashiro, S. 2011, *ApJ*, **736**, L17
- Gopalswamy, N., Yashiro, S., Akiyama, S., et al. 2008b, *Ann. Geophys.*, **26**, 3033
- Gopalswamy, N., Yashiro, S., Michalek, G., et al. 2009b, *Earth Moon Planets*, **104**, 295
- Gopalswamy, N., Yashiro, S., Xie, H., et al. 2008c, *ApJ*, **674**, 560
- Gosling, J. T., Hildner, E., MacQueen, R. M., et al. 1974, *J. Geophys. Res.*, **79**, 4581
- Hayes, A. P., Vourlidas, A., & Howard, R. A. 2001, *ApJ*, **548**, 1081
- Ingleby, L. D., Spangler, S. R., & Whiting, C. A. 2007, *ApJ*, **668**, 520
- Kozarev, K. A., Korreck, K. E., Lobzin, V. V., Weber, M. A., & Schwadron, N. A. 2011, *ApJ*, **733**, L25
- Landau, L. D., & Lifshitz, E. M. 1959, *Fluid Mechanics* (New York: Pergamon)
- LeBlanc, Y., Dulk, G. A., & Bougeret, J.-L. 1998, *Sol. Phys.*, **183**, 165
- Lee, J., White, S. M., Kundu, M. R., Mikic, Z., & McClymont, A. N. 1999, *ApJ*, **510**, 413
- Lin, H., Penn, M. J., & Tomczyk, S. 2000, *ApJ*, **541**, L83
- Liu, Y., Richardson, J. D., Belcher, J. W., & Kasper, J. C. 2006, *J. Geophys. Res.*, **111**, A01102
- Ma, S., Raymond, J. C., Golub, L., et al. 2011, *ApJ*, **738**, L60
- Maloney, S. A., & Gallagher, P. T. 2011, *ApJ*, **736**, L5
- Manchester, W. B., IV 2009, *BAAS*, **41**, 858
- Manchester, W. B., IV, Gombosi, T. I., Rousev, I., et al. 2004, *J. Geophys. Res.*, **109**, A02107
- Mann, G., Aurass, H., Klassen, A., Estel, C., & Thompson, B. J. 1999, in 8th SOHO Workshop, Plasma Dynamics and Diagnostics in the Solar Transition Region and Corona, ed. J.-C. Vial & B. Kaldeich-Schumann (ESA SP-446; Noordwijk: ESA), 477
- Michels, D. J., Sheeley, N. R., Jr., Howard, R. A., et al. 1984, *Adv. Space Res.*, **4**, 311
- Newkirk, G. 1961, *ApJ*, **133**, 983
- Ontiveros, V., & Vourlidas, A. 2009, *ApJ*, **693**, 267
- Patzold, M., Bird, M. K., & Volland, H. 1987, *Sol. Phys.*, **109**, 91
- Ramesh, R., Kathiravan, C., & Sastry, Ch. V. 2010, *ApJ*, **711**, 1029
- Russell, C. T., & Mulligan, T. 2002, *Planet. Space Sci.*, **50**, 527
- Seiff, A. 1962, *Gasdynamics in Space Exploration*, NASA Spec. Publ. 24
- Sheeley, N. R., Jr., Hakala, W. N., & Wang, Y.-M. 2000, *J. Geophys. Res.*, **105**, 5081
- Sheeley, N. R., Jr., Wang, Y.-M., Hawley, S. H., et al. 1997, *AJ*, **484**, 472
- Smerd, S. F., Sheridan, K. V., & Stewart, R. T. 1974, in IAU Symp. 57, Coronal Disturbances, ed. G. A. Newkirk (Dordrecht: Reidel), 389
- Solanki, S. K., Lagg, A., Woch, J., Krupp, N., & Colladis, M. 2003, *Nature*, **425**, 692
- Spangler, S. R. 2005, *Space Sci. Rev.*, **121**, 189
- Stepanova, T. V., & Kosovichev, A. G. 2000, *Adv. Space Res.*, **25**, 1855
- Van de Hulst, H. C. 1950, *Bull. Astron. Inst. Neth.* **XI**, 410, 135
- Vourlidas, A., Wu, S. T., Wang, A. H., Subramanian, P., & Howard, R. A. 2003, *ApJ*, **598**, 1392
- Vrsnak, B., Magdalenic, J., & Zlobec, P. 2004, *A&A*, **413**, 753
- Wiegelmann, T. 2008, *J. Geophys. Res.*, **113**, A03S02
- Yashiro, S., Gopalswamy, N., Michalek, G., et al. 2004, *J. Geophys. Res.*, **109**, 7105